

## Battery integrated three input high gain dc-dc converter for renewable energy sources

Azuka Affam<sup>1</sup>, Yonis M. Yonis Buswig<sup>2</sup>, Al-khalid bin Hj Othman<sup>1</sup>, Shanti Farida Salleh<sup>2</sup>, Hazrul Mohamed Basri<sup>1</sup>, Norhuzaimin bin Julai<sup>1</sup>, Kasumawati Lias<sup>2</sup>

<sup>1</sup>Department of Electrical and Electronic Engineering, Faculty of Engineering, Universiti Malaysia Sarawak, Kota Samarahan, Malaysia

<sup>2</sup>Institute of Sustainable and Renewable Energy (ISuRE), Faculty of Engineering, Universiti Malaysia Sarawak, Kota Samarahan, Malaysia

### Article Info

#### Article history:

Received mm dd, yyyy

Revised mm dd, yyyy

Accepted mm dd, yyyy

#### Keywords:

Boost converter

High gain

Multiple input

Non-coupled inductor

Renewable energy

### ABSTRACT

In this work, a battery integrated three input converter is proposed. The topology combines a traditional boost converter on one side with a non-coupled inductor-based buffer stage on the other side. Some merits of the converter are a high voltage gain, high output voltage in the battery discharging mode, and a wide range of output voltage. The bidirectional port makes it attractive for renewable energy (RE) sources like solar and fuel cell. The converter can operate in three modes that are determined by the availability of RE sources and the battery state of charge (SOC). The power management algorithm enabled the converter to work in either single input, double input or three input configurations. The duty ratios of assigned power switches controlled the output voltage and the battery charge/discharge. Steady-state analyses, and the dynamic modeling are presented and discussed. At 12 V and 24 V input voltage, output voltage of 315.52 V was delivered in the battery excluded mode. The battery discharging mode delivered 311.57 V while the battery charging mode delivered 301.32 V. The proposed converter can serve low to medium power voltage/ power applications. The hardware experiments verify the workings of the proposed converter.

*This is an open access article under the [CC BY-SA](#) license.*



### Corresponding Author:

Azuka Affam

Department of Electrical and Electronic Engineering, Faculty of Engineering, Universiti Malaysia Sarawak  
Kota Samarahan, Sarawak, Malaysia

Email: 18010014@siswa.unimas.my

## 1. INTRODUCTION

The adoption of RE sources has been on the increase in recent times. The major driving force behind the agitation of utilization of RE sources is the call to scale down the emission of greenhouse gases from the burning of fossil fuels [1]. It has also been determined that fossil fuel reserves are gradually diminishing [2]. The pursuit of cleaner sustainable energy resources does not end in the power generation sector. Studies show that the transportation sector contributes significantly to environmental pollution [3]. Although hybrid electric vehicles are gradually gaining ground, efforts are directed at summarily replacing gasoline vehicles with the electric vehicle alternatives in the coming decades via legislation. Unfortunately, the RE sources face impediments to their optimal power delivery and performance. Their electrical characteristic waver with time, and availability relies on factors like sun irradiance, ambient temperature, wind speed profile, or water velocity [4]. These variations result in low voltage levels.

A scheme to mitigate the dilemma of capricious power delivery faced by RE sources is to incorporate more than one RE source to improve reliability. Regarding the low output voltage of RE sources, the dc-dc

converters take center stage in power conversion to deliver regulated power to the load. They can step up or step-down voltage levels as desired. Conventionally, applications of dc-dc converters are in single input source scenario. With the demerits of RE sources, using multiple RE input sources demands a multiple input converter (MIC). In the early MIC, all input sources have their dedicated dc-dc converter, and the respective outputs are linked to a common DC bus. Apart from the bulky nature and high cost of such setup, this configuration faces problems of difficult switching, voltage, and current control. For the contemporary multiple input dc-dc converter, the independent RE sources are conducted to a single dc-dc converter. This results in reduced cost and size. Hence the MIC receives energy from all the input sources and deliver power to the load as desired, irrespective of the individual RE voltage levels. The MIC is widely used due to its capability to draw power individually and simultaneously from RE sources and deliver to a load.

A multiple input converter that eliminates the deployment of an inductor in the topology was been proposed in [5], [6]. This topology employed the switched capacitors technique. While this converter achieved reduced voltage and current stresses, high output ripple and output leakage voltage persist. In [7], [8], a lone inductor has been added before the switched-capacitor-diode configuration. The high voltage gain was achieved in [9] by using coupled inductors and a clamping circuit. The high voltage gain MIC [10] can eliminate input current ripples and has low voltage stress. The MIC based on the flyback converter can deliver a high voltage gain in buck or boost mode [11]. The output voltage is non-inverted.

The double input converter in [12], applied the boost cascaded charge pump method. It has the advantage of continuous current on the input ports, which is good for photovoltaic source. A Z-Quasi Resonant network was proposed to reduce the voltage stress of the dual input converter [13]. The converter is suitable for electric vehicles and microgrids. The converter introduced in [14] is suitable for PV storage. Two unidirectional ports suffice. Buck and buck-boost techniques are used at the energy buffer stage.

The application of voltage multiplier cell as a means of attaining high voltage gain in MICs has been investigated [15]. The voltage multiplier stages follow an interleaved boost stage. A bidirectional function for a storage element was added [16] by looping a battery based PVSC input. In [17], multiple output ports were added after the diode-capacitor stages. These converters suffer from high dissipation loss due to the increased number of passive elements. To reduce losses, an auxiliary ZVT circuit was added [18]. The coupled inductor technique was used to facilitate ZCS [19].

A double input and double output boost converter has been proposed in [20]. The converter achieved acceptable efficiency. It however has a high number of passive components. A bridge-type double input topology was proposed in [21]. The boost converter has a simple structure and low cost. Low voltage gain is a drawback of the converter. In [22], a switched inductor module positioned after the dual input stage was employed to improve the voltage gain. In the modular converter proposed in [23], each additional input port is connected to an interleaved inductor branch in a cascaded structure. The primary input port is a boost converter lifted by a capacitor. It has a low voltage stress. The MICs discussed in [5]–[23] have no directional battery port. As such they cannot serve the load when all the RE sources are low in power.

For MICs having a battery storage, [24] has a low voltage gain and the battery can only be charged by one RE source. The modular switched inductors was investigated in the multi-input boost converter [25]. The drawback is increased size and cost. Another converter that possesses an energy storage element has been adapted for PV, fuel cell and battery inputs [26]. It used a buck-boost configuration on one unidirectional input, and the boost configuration on the other input. In [27], the boost configuration was used on both inputs to ensure continuous input current for RE sources. Some weaknesses of these converters are the low voltage gain especially in the battery discharging mode. There is also low efficiency due to passive elements. The output voltage of the converters in [24]–[27] during the battery discharging mode, is lower.

This work proposes a non-coupled inductor / boost converter configuration to achieve high voltage gain for the operation modes of the battery integrated three-input converters highlighted in the literature. Existing literature have ignored the output voltage during battery discharging operation. The proposed converter combines two RE sources and a battery. The non-coupled inductor configuration helps deliver wide output voltage range and high voltage output despite the reduced input power levels in the battery discharging mode. This paper is organized as follows. The background and literature review are presented in the first section. The second section shows the proposed converter, steady-state analysis, dynamic modeling, and power management. Experimental results and comparisons are shown and discussed in the third section. Section four provides conclusions to the paper.

## 2. METHOD

In this section, the configuration of the proposed converter will be presented. In addition, the operation modes and respective switching states will be discussed. The section will conclude with the steady-state analysis, component design, dynamic modelling and power management algorithm.

## 2.1. Topology of the proposed converter

The proposed structure is presented in Figure 1(a). The right side of this converter is a conventional boost converter. On the left side is a non-coupled inductor-based converter configuration. There are three inputs that can be identified as  $V_1$ ,  $V_2$  and  $V_b$ .  $V_1$  is tied to the simple boost converter,  $V_2$  serves the uncoupled inductor-based converter.  $V_b$  is a battery source sandwiched between the two component converters. There are four power switches,  $S_1$ ,  $S_2$ ,  $S_3$  and  $S_4$  in the circuit. Switches,  $S_1$  and  $S_2$  serve the conventional boost converter and the non-coupled inductor-based boost converter respectively. Switches  $S_3$  and  $S_4$  serve to charge or discharge the battery as well as complete the flow of current. Other components of the converter include three inductors ( $L_1$ ,  $L_2$ ,  $L_3$ ), five diodes ( $D_o$ ,  $D_1$ ,  $D_{b1}$ ,  $D_{b2}$ ,  $D_m$ ), and four capacitors ( $C_o$ ,  $C_1$ ,  $C_2$ ,  $C_3$ ). While the traditional boost converter delivers voltage as expected, the non-coupled inductor/capacitor pairing contributes to producing greater output voltage. This inductor/capacitor pair is formed by inductors  $L_2$ ,  $L_3$ , and capacitors,  $C_2$ ,  $C_3$ . Diode  $D_m$  is dedicated to freewheeling purposes.

## 2.2. Operation mode one (Battery bypassed)

The first operation mode occurs when the supply voltage for  $V_1$  and  $V_2$  can satisfy the existing load. This mode of operation involves four switching states. Also at this point, the battery is fully charged. The battery is cut off by turning off either pair of  $S_4$  and  $D_{b1}$  or  $S_3$  and  $D_{b2}$ . The switching states are described.

- Switching state 1 ( $t_0 - t_1$ ):  $S_1$ ,  $S_2$  and  $S_3$  are turned on.  $S_4$  stays turned off with  $D_{b1}$  to cut off supply to the battery. The equivalent circuit is depicted in Figure 1(b).  $L_1$  is charged by  $V_1$  through  $S_1$ . Similarly,  $L_2$  is charged by  $V_2$  through  $S_2$ .  $C_3$  charges  $L_3$  and  $C_2$ .  $C_1$  is in idle state.  $C_o$  serves the load during this switching state.  $D_o$ ,  $D_1$ , and  $D_m$  do not conduct.
- Switching state 2 ( $t_1 - t_2$ ): The circuit is illustrated in Figure 1(c).  $S_1$  is turned off while  $S_2$  stays on like previously.  $D_o$  conducts hence  $L_1$  and  $C_1$  discharge in consonance with  $V_1$  to deliver energy to the load.
- Switching state 3 ( $t_2 - t_3$ ): The circuit is as shown in Figure 1(d).  $S_1$  is turned on,  $S_2$  and  $S_3$  are turned off.  $S_4$  and  $D_{b1}$  conduct.  $D_o$  is turned off while  $D_1$  and  $D_m$  conduct.  $L_1$  is charged by  $V_1$ .  $C_3$  is charged by  $V_2$  and  $L_2$ .  $L_3$  charges  $C_1$  and  $C_o$  serves the load.
- Switching state 4 ( $t_3 - T$ ):  $S_1$  and  $S_2$  are turned on.  $D_o$  is turned off. The components exhibit the same pattern as in switching state 1.  $C_o$  serves the load. The relevant equations are;

$$L_2: V_2 d_2 T_s + V_2 - V_{C3}(1 - d_2) T_s = 0 \quad (1)$$

$$L_2: V_2 d_2 T_s + V_2 + V_{C2} - V_{C1}(1 - d_2) T_s = 0 \quad (2)$$

$$L_1: V_1 d_1 T_s + V_1 + V_{C1} - V_o(1 - d_2) T_s = 0 \quad (3)$$

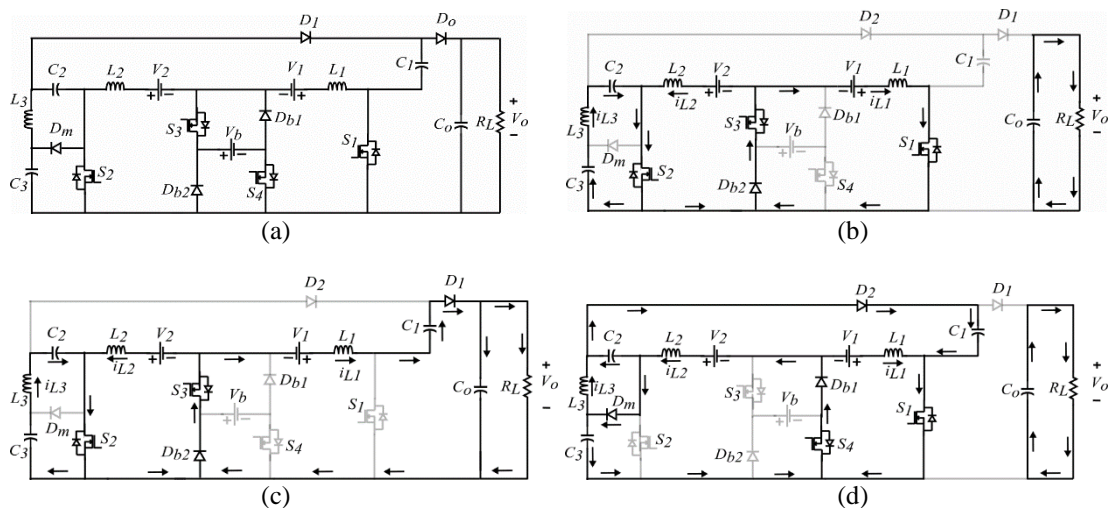


Figure 1. Proposed converter and operation mode 1 current paths (a) proposed converter, (b) switching state 1, (c) switching state 2, and (d) switching state 3

$$V_{C3} = \frac{2V_2}{1-d_2} \quad (4)$$

$$V_{C2} = \frac{3V_2}{2-2d_2} \quad (5)$$

$$V_{C1} = \frac{3V_2}{2-2d_2} + \frac{2V_2}{1-d_2} \quad (6)$$

$$V_o = \frac{V_1 + (V_{C1}(1-d_1))}{1-d_1} \quad (7)$$

$$G_V = \frac{V_o}{V} = \frac{1 + \left(\frac{3}{2-2d_2} + \frac{2}{1-d_2}\right)(1-d)}{1-d} \quad (8)$$

Where,  $d_1$  is the duty ration of switch  $S_1$ ;  $d_2$  is the duty ratio of switch  $S_2$ ;  $V_{C1}$  is the voltage across capacitor  $C_1$ ;  $V_{C2}$  is the voltage across capacitor  $C_2$ ;  $V_{C3}$  is the voltage across capacitor  $C_3$ ;  $T_s$  is the total period;  $V_o$  is the output voltage; and  $G_V$  is the voltage gain.

### 2.3. Operation mode two (Battery discharging)

In this operation mode, the load cannot be served by the RE sources alone. Hence, the battery storage,  $V_b$  is engaged to support the power delivered to the load.  $S_3$  and  $S_4$  play the role of allowing or disallowing the battery to deliver power to the load.  $S_3$  is perpetually turned on during this operation mode. The respective switching states are described hereafter.

- Switching state 1 ( $t_0 - t_1$ ): The circuit is represented in Figure 2(a). All switches are turned on.  $D_{b1}$  and  $D_{b2}$  are turned off.  $V_b + V_1$  charges  $L_1$  while  $V_b + V_2$  charges  $L_2$ .  $C_1$  is idle.  $D_o$  and  $D_1$  are off.  $C_o$  delivers power to the load.
- Switching state 2 ( $t_1 - t_2$ ): The equivalent circuit is shown in Figure 2(b).  $S_1$  is turned off while all other switches stay on.  $V_b + V_1 + V_{C1}$  supplies power to the load via  $D_o$ .
- Switching state 3 ( $t_2 - t_3$ ): The circuit is shown in Figure 2(c).  $S_3$  and  $S_4$  remain turned.  $V_b$  charges  $L_1$  and  $L_2$ .
- Switching state 4 ( $t_3 - T$ ): Switching state 4 of operation mode 1 is replicated here. Relevant equations are;

$$L_2: V_2 d_2 T_s + V_b d_4 T_s - V_2 + V_b d_4 - V_{C3}(1-d_2)T_s = 0 \quad (9)$$

$$L_2: V_2 d_2 T_s + V_b d_4 T_s + V_b d_4 + V_2 + V_{C2} - V_{C1}(1-d_2)T_s = 0 \quad (10)$$

$$L_1: V_1 d_1 T_s + V_b d_4 - V_b d_4 + V_1 + V_{C1} - V_o(1-d_1)T_s = 0 \quad (11)$$

$$i_b = d_4(i_{L1} + i_{L2} + i_{L3}) \quad (12)$$

$$P_b = V_b(d_4(i_{L1} + i_{L2} + i_{L3})) \quad (13)$$

$$V_{C3} = \frac{V_b(1+d_4) + V_2(1+d_2)}{1-d_2} \quad (14)$$

$$V_{C2} = \frac{V_2(2+d_2) + V_b(2-d_2+2d_4)}{2-2d_2} \quad (15)$$

$$V_{C1} = \frac{V_b(1+d_4) + V_2(1+d_2)}{1-d_2} + \frac{V_2(2+d_2) + V_b(2-d_2+2d_4)}{2-2d_2} \quad (16)$$

$$V_o = \frac{V_1 + (V_b(1-d_1+d_4)) + (V_{C1}(1-d_1))}{1-d_1} \quad (17)$$

Where,  $d_4$  is the duty ratio of switch  $S_4$ ;  $i_b$  is the battery current;  $P_b$  is the battery power;  $i_{L1}$  is the current for inductor  $L_1$ ;  $i_{L2}$  is the current for inductor  $L_2$ ; and  $i_{L3}$  is the current for inductor  $L_3$ .

### 2.4. Operation mode three (Battery charging)

In this working mode, the battery state of charge (SOC) is low and the RE sources have the capacity to charge the battery while serving the load. Switch  $S_4$  regulates the charging of the battery.  $S_3$  is turned off during this operation mode. The switching modes are described.

- Switching state 1 ( $t_0 - t_1$ ): Switching state 1 of operation mode one is replicated here. No battery charging.
- Switching state 2 ( $t_1 - t_2$ ): Switching state 2 of operation mode one is repeated here. No battery charging.
- Switching state 3 ( $t_2 - t_3$ ): The circuit is shown in Figure 2(d). Only  $S_2$  is turned on.  $D_{b1}$  and  $D_{b2}$  conduct.  $V_b$  is charged along with  $C_3$  by both  $V_1$ ,  $V_2$ , and energy discharged from  $L_2$ .  $C_o$  deliver power to the load.
- Switching state 4 ( $t_3 - T$ ): Switching state 4 of the first operation mode is replicated. No battery charging. The equations are;

$$L_2: V_2 d_2 T_s - (V_2 - V_{C3} - V_b(1 - d_4))(1 - d_2) T_s = 0 \quad (18)$$

$$L_2: V_2 d_2 T_s + V_2 + V_{C2} - V_{C1}(1 - d_2) T_s = 0 \quad (19)$$

$$L_1: V_1 d_1 T_s - V_b(d_1 - d_4) - V_1 + V_{C1} - V_o(1 - d_1) T_s = 0 \quad (20)$$

$$i_b = i_{L1}(d_1 - d_4) + i_{L2} + i_{L3}(d_2 - d_4) \quad (21)$$

$$P_b = V_b(i_{L1}(d_1 - d_4) + i_{L2} + i_{L3}(d_2 - d_4)) \quad (22)$$

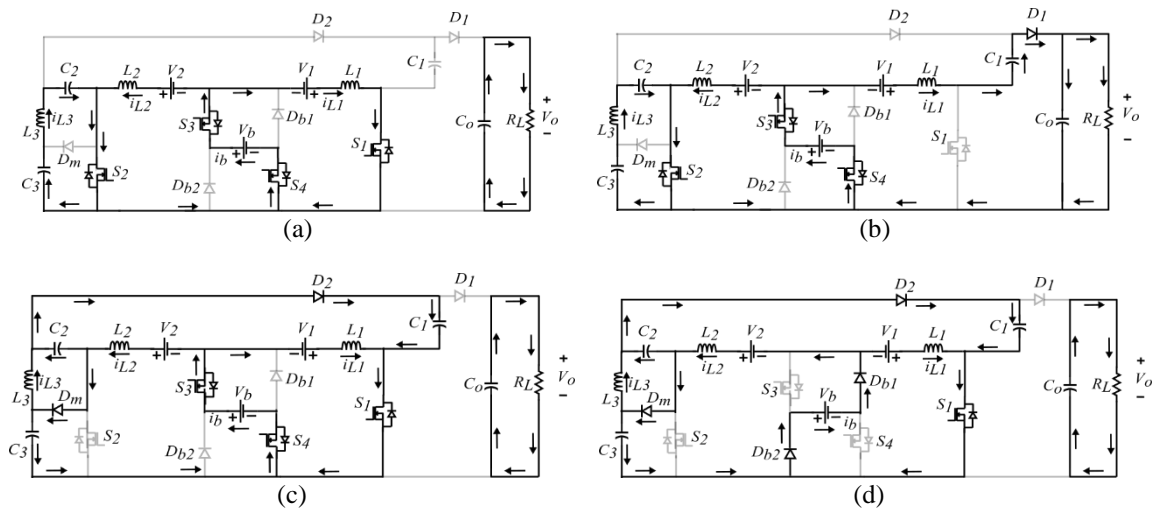


Figure 2. Current paths for operation modes 2 and 3 (a) switching state 1, (b) switching state 2, (c) switching state 3, and (d) switching state 3 of operation mode 3

$$V_{C3} = \frac{V_2 + V_b(1 - d_2 + d_4 + d_2 d_4)}{1 - d_2} \quad (23)$$

$$V_{C2} = \frac{V_2 + V_{C3}(1 - d_2)}{2 - 2d_2} \quad (24)$$

$$V_{C1} = \frac{V_2 + \frac{V_2 + V_b(1 - d_2 + d_4 + d_2 d_4)}{1 - d_2}}{2 - 2d_2} + \frac{V_2 + V_b(1 - d_2 + d_4 + d_2 d_4)}{1 - d_2} \quad (25)$$

$$V_o = \frac{V_1 + (V_b(d_1 - d_4)) + (V_{C1}(1 - d_1))}{1 - d_1} \quad (26)$$

Figure 3(a) shows the switching pattern for operation mode one. The switching patterns for modes two and three are depicted in Figure 3(b) and Figure 3(c) respectively. The waveforms of the inductor currents and capacitor voltages are shown in Figure 3(d).

## 2.5. Design of inductors and capacitors

The design of the inductors is akin to that of the conventional boost converter. To ensure continuous conduction mode (CCM), the inductor average current must be greater than half of the inductor ripple current. Hence, for inductors  $L_1$  and  $L_2$

$$I_{L1} \geq \frac{\Delta i_{L1}}{2}, I_{L2} \geq \frac{\Delta i_{L2}}{2} \quad (27)$$

By applying ampere-second balancing on the respective capacitors, the average current of  $L_1$  and  $L_2$  are  $I_{L1}$  and  $I_{L2}$  respectively. These depend on the output current,  $I_o$  and duty ratio of the switches and is expressed as

$$I_{L1} = \frac{2I_o}{1-d_1}, I_{L2} = \frac{4I_o}{1-d_2} \quad (28)$$

The inductor currents of the boost and non-coupled inductor sides of the converter are shown by (27) and (28) can be controlled by varying  $d_1$  and  $d_2$  respectively. In addition, the average current of  $L_3$  is the same as the output current of the converter.

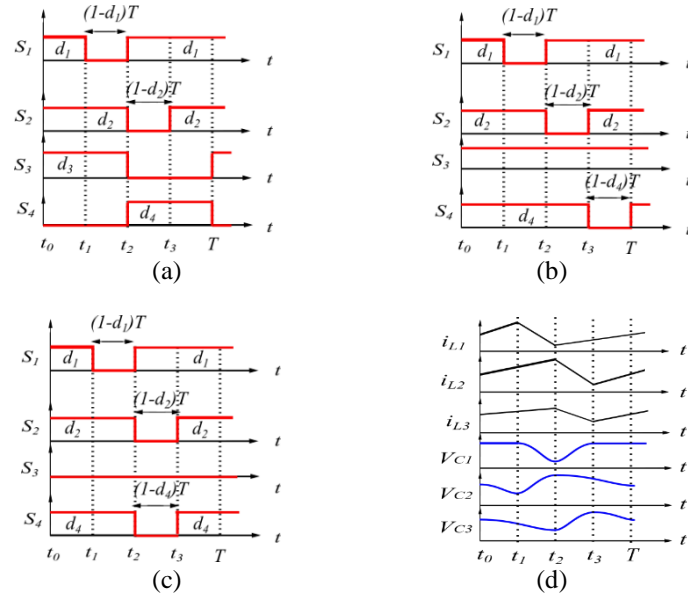


Figure 3. Key waveforms (a) mode 1, (b) mode 2, (c) mode 3 and (d)  $i_{L1}$ ,  $i_{L2}$ ,  $i_{L3}$ ,  $V_{C1}$ ,  $V_{C2}$  &  $V_{C3}$

In calculating the minimum value of the inductors, the second operation mode is to be considered. This is because  $V_1$  and  $V_2$  generate the lowest energy in this mode. Such a scenario could result in the converter operating in discontinuous conduction mode (DCM). The inductors' current ripples in the second operation can be found as

$$\Delta i_{L1} = \frac{d_1 V_1 + d_4 V_b}{L_1 f_s}, \Delta i_{L2} = \frac{d_2 V_2 + d_4 V_b}{L_2 f_s} \quad (29)$$

Hence, the values of the inductors,  $L_1$ ,  $L_2$  and  $L_3$  can be obtained as

$$L_1 \geq \frac{d_1 V_1 + d_4 V_b}{\Delta i_{L1} f_s}, L_2 = L_3 \geq \frac{d_2 V_2 + d_4 V_b}{\Delta i_{L2} f_s} \quad (30)$$

It can be seen from (29) and (30) that the required inductance reduces when the switching frequency,  $f_s$  is increased. In practice, the higher inductance values are applied to reduce the inductor ripple current.

In order to properly design the converter, it is essential that the voltage and current stress of the semiconductor devices are taken into cognizance. The voltage stress of the device is also known as peak inverse voltage. It is the maximum voltage encountered by the device without being destroyed when it is turned off. During CCM, the voltage stress and current stress of the devices are given in Table 1.

It is vital that the capacitors,  $C_o$ ,  $C_1$ ,  $C_2$  and  $C_3$  can permit a change in the charge and voltage variations during their respective charging ranges. To ensure CCM, the inductor average current must be greater than half of the inductor ripple current.

The capacitances can be obtained by

$$C_1 \geq \frac{2i_o}{f_s(1-d_1)\Delta V_{C1}}, C_2 = C_3 \geq \frac{i_{L2} - i_o}{f_s(1-d_1)\Delta V_{C2,3}}, C_o \geq i_o \frac{d_1}{f_s \Delta V_{C_o}} \quad (31)$$

Table 1. Voltage and current stress of the devices

Device	Voltage stress	Device	Current stress
$S_1, D_1$	$V_o - V_{C1}$	$S_1$	$I_{L1max} + I_{L2max}$
$S_2, D_m$	$V_{C3}$	$S_2$	$I_{L2max} + I_{L3max}$
$D_2$	$V_o - V_{C1} + V_{C3}$	$S_3, D_3$	$I_{L1max} + I_{L2max} + I_{L3max}$
$S_3, S_4, D_3, D_4$	$V_{FD}$	$D_1$	$I_{L1}$
		$D_2$	$I_{L2} + I_{L3}$
		$D_m$	$I_{L2} + I_{L3} - I_{L1}$

## 2.6. Dynamic model of the converter

The first operation mode uses two active-duty ratios ( $d_1, d_2$ ), while the second and third operating modes use three alternate duty ratios ( $d_1, d_2, d_4$ ). The topology description indicates that there are seven passive elements in the proposed converter. These are  $L_1, L_2, L_3, C_1, C_2, C_3$ , and  $C_o$ . There are six state variables adopted. These are  $L_1, L_2, C_1, C_2, C_3$ , and  $C_o$ .

In performing small-signal modelling, it is assumed that two components make up the state variables, duty ratios, and input voltages (Nejabatkhah et al., 2012). These are perturbations ( $\tilde{x}, \tilde{d}, \tilde{v}$ ) and dc values ( $\bar{X}, \bar{D}, \bar{V}$ ) expressed as;

$$x = \bar{X} + \tilde{x}; d = \bar{D} + \tilde{d}; v = \bar{V} + \tilde{v} \quad (32)$$

By ignoring the second-order elements and assuming that the perturbations are modest and do not change dramatically over the course of a single switching period, small-signal models are produced. The small-signal models in matrix form are as follows;

$$\dot{x} = A\tilde{x} + B\tilde{u}, y = C\tilde{x} + D\tilde{u} \quad (33)$$

In (33),  $\tilde{x}$  is the state variable vector,  $\tilde{u}$  is the control variables vector and  $\tilde{y}$  is the output vector. The matrix forms of the small-signal models are presented.

For the first operation mode, the small-signal model is;

$$A = \begin{bmatrix} 0 & 0 & \frac{1-\bar{D}_1}{L_1} & 0 & 0 & \frac{\bar{D}_1-1}{L_1} \\ 0 & 0 & 0 & 0 & \frac{\bar{D}_2-1}{L_2} & 0 \\ \frac{1-\bar{D}_2}{C_1} & \frac{1-\bar{D}_2}{C_1} & 0 & 0 & 0 & \frac{2-2\bar{D}_1}{R_L C_1} \\ \frac{\bar{D}_2}{C_2} & \frac{2\bar{D}_2-2}{C_2} & 0 & 0 & 0 & 0 \\ -\frac{\bar{D}_2}{C_3} & \frac{1-\bar{D}_2}{C_3} & 0 & 0 & 0 & 0 \\ \frac{2-2\bar{D}_1}{C_o} & 0 & 0 & 0 & 0 & -\frac{1}{R_L C_o} \end{bmatrix}, B = \begin{bmatrix} \frac{\bar{V}_o - \bar{V}_{C1}}{L_1} & 0 \\ 0 & \frac{\bar{V}_{C3}}{L_2} \\ \frac{\bar{I}_{L1}}{2C_1} & \frac{\bar{I}_{L2} - \bar{I}_{L1}}{C_1} \\ 0 & \frac{2\bar{I}_{L2}}{C_2} \\ 0 & -\frac{\bar{I}_{L2}}{C_3} \\ -\frac{\bar{I}_{L1}}{C_o} & 0 \end{bmatrix} \quad (34)$$

$$C = \begin{bmatrix} 1 & 0 & 0 & 0 & 0 & 0 \\ 0 & 0 & 0 & 0 & 0 & 1 \end{bmatrix}, \tilde{x} = \begin{bmatrix} \tilde{I}_{L1} \\ \tilde{I}_{L2} \\ \tilde{V}_{C1} \\ \tilde{V}_{C2} \\ \tilde{V}_{C3} \\ \tilde{V}_o \end{bmatrix}, \tilde{u} = \begin{bmatrix} \tilde{d}_1 \\ \tilde{d}_2 \end{bmatrix}, D = 0 \quad (35)$$

For the second operation mode, the small-signal model is;

$$A = \begin{bmatrix} 0 & 0 & \frac{1-\bar{D}_1}{L_1} & 0 & 0 & \frac{\bar{D}_1-1}{L_1} \\ 0 & 0 & 0 & 0 & \frac{\bar{D}_2-1}{L_2} & 0 \\ \frac{1-\bar{D}_2}{C_1} & \frac{1-\bar{D}_2}{C_1} & 0 & 0 & 0 & \frac{2-2\bar{D}_1}{R_L C_1} \\ \frac{\bar{D}_2}{C_2} & \frac{2\bar{D}_2-2}{C_2} & 0 & 0 & 0 & 0 \\ -\frac{\bar{D}_2}{C_3} & \frac{1-\bar{D}_2}{C_3} & 0 & 0 & 0 & 0 \\ \frac{2-2\bar{D}_1}{C_o} & 0 & 0 & 0 & 0 & -\frac{1}{R_L C_o} \end{bmatrix}, B = \begin{bmatrix} \frac{\bar{V}_O - \bar{V}_{C1}}{L_1} & 0 & \frac{2\bar{V}_B}{L_1} \\ 0 & \frac{\bar{V}_{C3}}{L_2} & \frac{\bar{V}_B}{L_2} \\ \frac{\bar{I}_{L1}}{2C_1} & \frac{\bar{I}_{L2} - \bar{I}_{L1}}{C_1} & 0 \\ 0 & \frac{2\bar{I}_{L2}}{C_2} & 0 \\ 0 & -\frac{\bar{I}_{L2}}{C_3} & 0 \\ -\frac{\bar{I}_{L1}}{C_o} & 0 & 0 \end{bmatrix} \quad (36)$$

$$C = \begin{bmatrix} 1 & 0 & 0 & 0 & 0 & 0 \\ 0 & 1 & 0 & 0 & 0 & 0 \\ 0 & 0 & 0 & 0 & 0 & 1 \end{bmatrix}, \tilde{x} = \begin{bmatrix} \tilde{I}_{L1} \\ \tilde{I}_{L2} \\ \tilde{V}_{C1} \\ \tilde{V}_{C2} \\ \tilde{V}_{C3} \\ \tilde{V}_o \end{bmatrix}, \tilde{u} = \begin{bmatrix} \tilde{d}_1 \\ \tilde{d}_2 \\ \tilde{d}_4 \end{bmatrix}, D = 0 \quad (37)$$

For the third operation mode, the small-signal model is;

$$A = \begin{bmatrix} 0 & 0 & \frac{1-\bar{D}_1}{L_1} & 0 & 0 & \frac{\bar{D}_1-1}{L_1} \\ 0 & 0 & 0 & 0 & \frac{\bar{D}_2-1}{L_2} & 0 \\ \frac{1-\bar{D}_2}{C_1} & \frac{1-\bar{D}_2}{C_1} & 0 & 0 & 0 & \frac{2-2\bar{D}_1}{R_L C_1} \\ \frac{\bar{D}_2}{C_2} & \frac{2\bar{D}_2-2}{C_2} & 0 & 0 & 0 & 0 \\ -\frac{\bar{D}_2}{C_3} & \frac{1-\bar{D}_2}{C_3} & 0 & 0 & 0 & 0 \\ \frac{2-2\bar{D}_1}{C_o} & 0 & 0 & 0 & 0 & -\frac{1}{R_L C_o} \end{bmatrix}, B = \begin{bmatrix} \frac{\bar{V}_O - \bar{V}_{C1} - \bar{V}_B}{L_1} & 0 & \frac{\bar{V}_1 - \bar{V}_B}{L_1} \\ 0 & \frac{\bar{V}_2}{L_2} & \frac{\bar{V}_2 - \bar{V}_{C3} - \bar{V}_B}{L_2} \\ \frac{\bar{I}_{L1}}{2C_1} & \frac{\bar{I}_{L2} - \bar{I}_{L1}}{C_1} & 0 \\ 0 & \frac{2\bar{I}_{L2}}{C_2} & 0 \\ 0 & -\frac{\bar{I}_{L2}}{C_3} & 0 \\ -\frac{\bar{I}_{L1}}{C_o} & 0 & 0 \end{bmatrix} \quad (38)$$

$$C = \begin{bmatrix} 1 & 0 & 0 & 0 & 0 & 0 \\ 0 & 1 & 0 & 0 & 0 & 0 \\ 0 & 0 & 0 & 0 & 0 & 1 \end{bmatrix}, \tilde{x} = \begin{bmatrix} \tilde{I}_{L1} \\ \tilde{I}_{L2} \\ \tilde{V}_{C1} \\ \tilde{V}_{C2} \\ \tilde{V}_{C3} \\ \tilde{V}_o \end{bmatrix}, \tilde{u} = \begin{bmatrix} \tilde{d}_1 \\ \tilde{d}_2 \\ \tilde{d}_4 \end{bmatrix}, D = 0 \quad (39)$$

## 2.7. Power Management Algorithm of the converter

It is crucial to create an algorithm to choose the proper operation mode for hybrid MICs. The first input port is the PV port, and the second input port is the FC port. The operation scenarios could happen if the PV produces insufficient electricity or if the load requirements are higher. As long as there is enough power in the battery storage and any of the input sources, the proposed converter should be able to handle the load.

Determining the minimal power levels necessary for the converter modes to function properly is crucial. The lowest power from the PV ( $P_{PV}$ ) and the power from the FC ( $P_{FC}$ ) are identified. Also, upper and lower SOC references ( $B_L$  and  $B_U$ ) are identified for the battery. The load power requirement,  $P_L$ , is considered. Figure 4 shows the proposed algorithm for the energy management. It is important to note that, the operating logic in the Figure 4 handles how an operation mode is chosen in the first instant. Switching between operation modes will depend on a monitoring circuit and battery management system which are not within the scope of this study.

The process for managing power is explained.

- When there is a reduced load,  $P_L$  is contrasted with either  $P_{PV}$  and  $P_{FC}$  or  $P_{PV} + P_{FC}$ .  $P_{PV}$  is given priority in the algorithm. The SOC is examined to see if it is more than  $B_U$  if  $P_{PV}$  is able to meet the load,  $P_L$ . The first operation mode kicks in when the SOC exceeds the  $B_U$  and bypasses the battery.
- When  $P_{PV}$ ,  $P_{FC}$ , or  $P_{PV} + P_{FC}$  cannot serve the load, the algorithm checks the SOC status. If  $SOC > B_U$ , the second operation mode is adopted and the battery discharges. It further checks if  $SOC < B_L$ . So long as  $SOC > B_L$ , the battery discharging mode continues. If  $SOC < B_L$ , the algorithm returns to the



start position or command.

- c. As can be seen from the algorithm, the third operation mode is adopted when  $P_{PV}$ ,  $P_{FC}$  or  $P_{PV} + P_{FC}$  is greater than  $P_L$  and  $SOC < B_L$ .

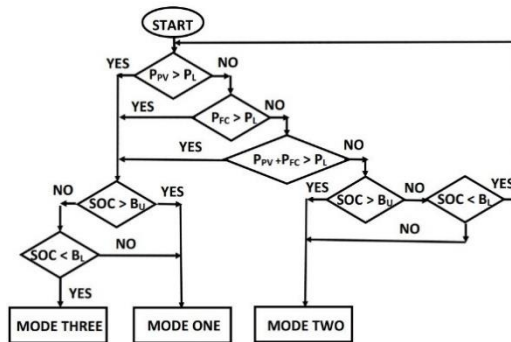


Figure 4. Algorithm for power management of the proposed converter

### 3. RESULTS AND DISCUSSION

In this section, the results will be presented. The output voltage range will also be established. Finally, the proposed converter will be compared with similar previous investigations.

#### 3.1. Experimental results

In validating the performance of the proposed converter, a hardware prototype has been implemented as depicted in Figure 5(a). RE sources,  $V_1$  at 12 V, and  $V_2$  at 24 V, were replicated by dc power supplies, while a 12 V rechargeable lead acid battery sufficed as the energy storage device. The dSPACE DS1104 digital controller board was used to generate the switching pulses for all the switches. In accordance with the derived equations, the other component ratings chosen as listed in Table 2. Switches  $S_1$  to  $S_4$  are Infineon G25H1203 IGBTs while the diodes are Cheng-Yi IN5400 axial silicon rectifier diodes. Based on (30), the critical inductances at chosen frequency of 15 kHz and 10 % ripple,  $L_1 \geq 300.6 \text{ mH}$ ,  $L_2 = L_3 \geq 157.6 \text{ mH}$  are obtained. Consequently,  $L_1 = 350 \text{ mH}$ ,  $L_2 = L_3 = 200 \text{ mH}$  are selected. For the capacitors, using (31) with permitted voltage ripple of 1%,  $C_1 \geq 78.1 \mu\text{F}$ ,  $C_2 \geq 42.5 \mu\text{F}$ ,  $C_3 \geq 31.8 \mu\text{F}$ , and  $C_o \geq 50 \mu\text{F}$  are selected. Hence,  $C_1 = C_2 = C_3 = 100 \mu\text{F}$  (100 uF, 400 V, Elite PF2G101MNN1832). The output capacitor,  $C_o = 270 \mu\text{F}$  (270uF 400 V, Nichicon LGL2G271MELZ35).

Table 2. Experimental parameters

Parameter	Value/ Part number
Input voltage	$V_1 = 12 \text{ V}$ , $V_2 = 24 \text{ V}$ , $V_b = 12 \text{ V}$
Frequency	15 kHz
Power switch	Infineon G25H1203 IGBT
Inductors	$L_1 = 350\text{mH}$ , $L_2, L_3 = 200\text{mH}$
Capacitors	$C_o = 270 \mu\text{F}$ , $C_1, C_2, C_3 = 100 \mu\text{F}$
Diodes	20A10 20A 1000V
Load	1000

At duty ratios of 0.75 and 0.7 for  $d_1$  and  $d_2$  respectively, the output voltage obtained in mode one is 315.53 V. Figure 5(b) shows  $V_1$ ,  $V_2$  and  $V_o$  during operation mode one. The duty ratios of  $S_3$  and  $S_4$  are set to 0.5 each. The capacitor voltages,  $V_{C1}$ ,  $V_{C2}$  and  $V_{C3}$  are shown in Figure 5(c). It can be seen that the voltages are 127.19 V for  $V_{C2}$ , 139.54 V for  $V_{C3}$ .  $V_{C1}$  is 266.69 V and is the sum of  $V_{C2}$  and  $V_{C3}$ .  $C_1$  is idle during the switching states 1 and 3. The waveforms of the inductor currents are presented in Figure 5(d). When  $S_1$  and  $S_2$  are conducting during the first switching state,  $i_{L1}$  and  $i_{L2}$  increase linearly as a result of the  $L_1$  and  $L_2$  being charged by  $V_1$  and  $V_2$  respectively. At  $t_2 - t_1$ ,  $i_{L1}$  decreases while  $i_{L2}$  and  $i_{L3}$  continue increasing. Inductor currents,  $i_{L2}$  and  $i_{L3}$  linearly decrease with a negative slope during the third switching state when  $S_2$  does not conduct while  $i_{L1}$  increases for two consecutive switching states. The approximate inductor currents are 2.12 A, 4.23 A and 0.305 A for  $i_{L1}$ ,  $i_{L2}$  and  $i_{L3}$  respectively.

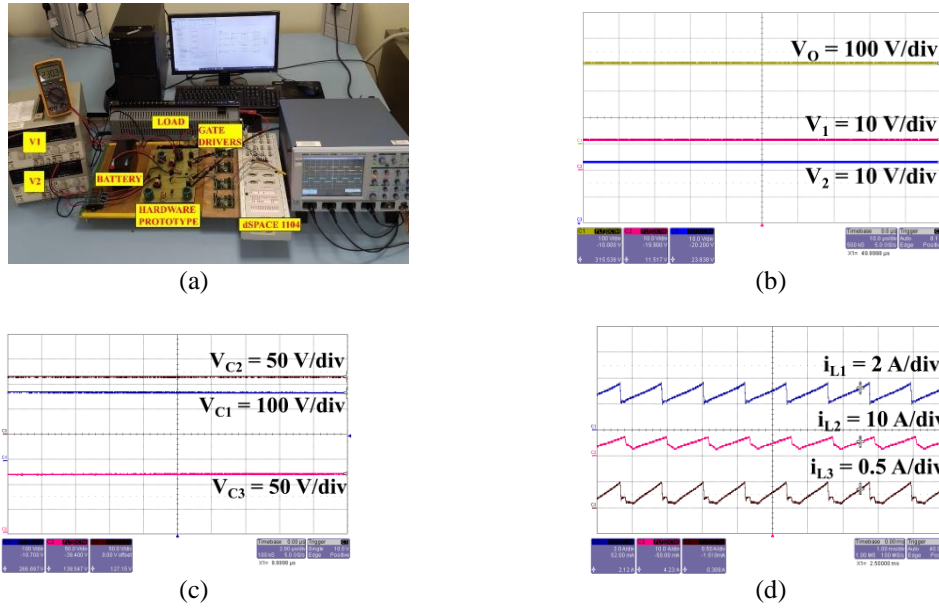


Figure 5. Operation mode 1 results (a) setup, (b)  $V_1$ ,  $V_2$  &  $V_o$  (c)  $V_{C1}$ ,  $V_{C2}$  &  $V_{C3}$  and (d)  $i_{L1}$ ,  $i_{L2}$  &  $i_{L3}$

The output voltage of the second operation mode is shown in Fig. 6(a).  $V_1$  and  $V_2$  have been reduced to 6 V and 12 V respectively. Duty ratios of 0.75, 0.7, and 0.75 for  $d_4$ ,  $d_2$  and  $d_1$  have been applied. The output voltage is 311.57 V. Since the same switching pattern is applied to  $S_1$  and  $S_2$  in all three operation modes, the

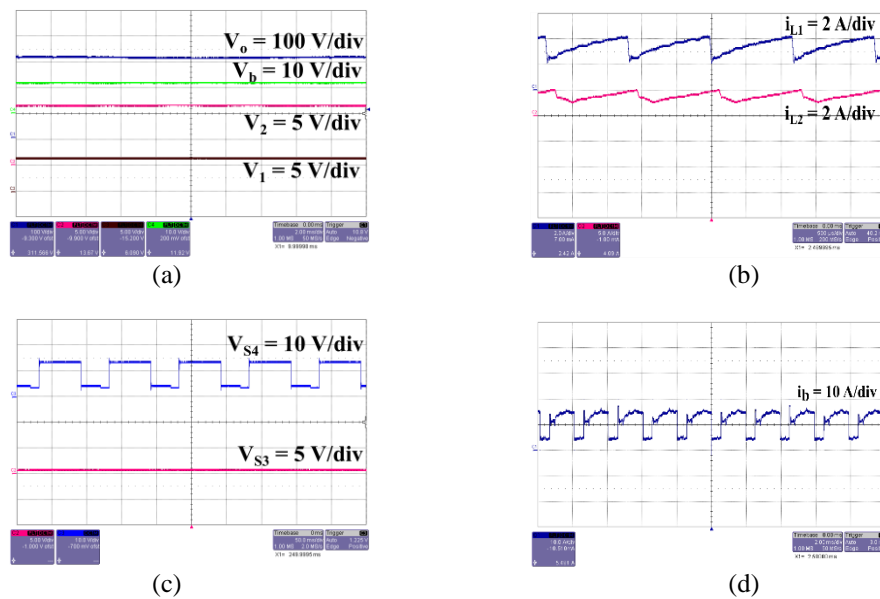


Figure 6. Operation mode 2 results (a)  $V_1$ ,  $V_2$ ,  $V_b$  &  $V_o$ , (b)  $i_{L1}$  &  $i_{L2}$ , (c)  $V_{S3}$  &  $V_{S4}$  and (d)  $i_b$

inductor currents ( $i_{L1}$ ,  $i_{L2}$ ,  $i_{L3}$ ), output current, capacitor voltages, switch voltage stress,  $V_{S1}$  and  $V_{S2}$ , for all the modes differ only in magnitude and not by waveform. The waveforms of  $i_{L1}$  and  $i_{L2}$  are shown in Figure 6(b). The voltage stress on  $S_3$  and  $S_4$  are shown in Figure 6(c).  $V_{S4}$  is equal to the battery supply voltage,  $V_b = 12$  V.  $V_{S3}$  is the forward voltage of 0.8 V. The battery current,  $i_b$  is displayed in Figure 6(d). It rises to about 5.49 A during the first three switching states and drops in the last state. It is the product of the duty ratio of switch,  $S_4$  by the summation of the inductor currents.

For the third operation mode, the duty ratio,  $d_4$  is set to 0.75. The measured output voltage is about 301.32 V. Figure 7(a) shows the output voltage, and the voltage on  $C_1$ . The voltage on  $C_1$  is about 277.69 V. While the converter serves the load, the battery is charged during the third switching state when there is a

negative slope on the signal. The voltage stress of the switches is shown in Fig 7(b). It can be observed that the appearance of the voltage across  $S_1$  occurs during the second switching state and during switching state three for  $S_2$ . The voltage stresses,  $V_{S1}$  and  $V_{S2}$ , across  $S_1$  and  $S_2$  are about 64.87 V and 119.54 V respectively.

The voltage stress on  $S_3$  and  $S_4$  is depicted in Figure 7(c).  $V_{S3}$  goes to zero in the third switching state and returns to about 10 V which is the voltage of the depleted battery. The voltage spike in  $V_{S3}$  occurs during switching state three when turning off  $S_3$  and  $S_4$  forces the current to charge the  $V_b$  through diodes,  $D_{b1}$  and  $D_{b2}$ . The  $i_{L1}$ ,  $i_{L2}$  and  $i_b$  are shown in Fig. 7(d). It indicates the spike in  $i_b$  to about 1 A when  $D_{b1}$  and  $D_{b2}$  conduct.

The experimentally output voltage range was measured. At  $V_1=12$  V,  $V_2=24$  V, the duty ratio  $d_1 = d_2 = d$ , was varied from 0.05 to 0.75. The output voltage ranges between 84 V and 381 V. The lowest voltage of 21.4 V was recorded when  $V_1$  is isolated at 0.05 duty ratio. This confirms the wide output voltage range of the proposed converter.

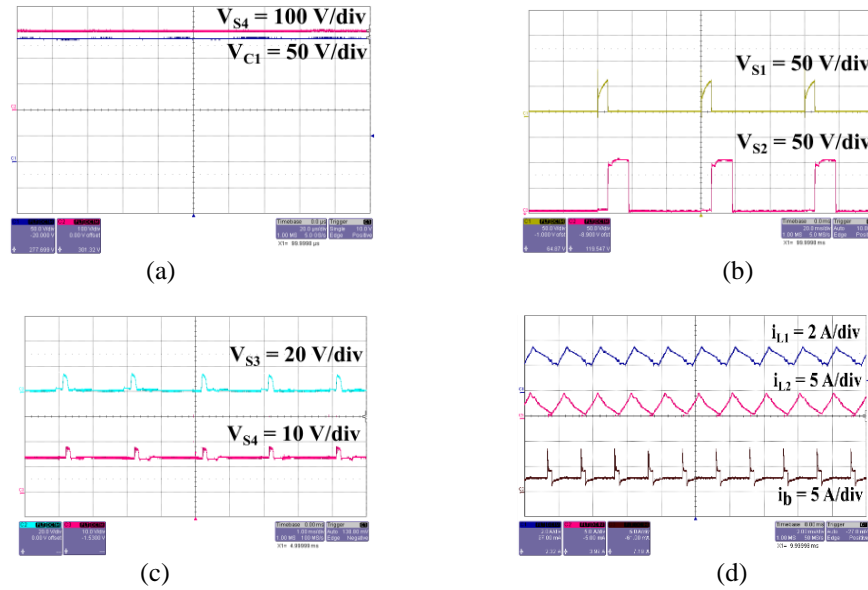


Figure 7. Operation mode 3 results (a)  $V_o$  &  $V_{C1}$ , (b)  $V_{S1}$  &  $V_{S2}$ , (c)  $V_{S3}$  &  $V_{S4}$ , and (d)  $i_{L1}$ ,  $i_{L2}$  &  $i_b$

### 3.3. Comparison with similar topologies

Table 3 shows a comparison of the proposed converter with similar topologies. Each of the compared converters has two input ports in addition to a battery port. The voltage gain and the number of components has been compared. The converters' voltage boosting method have been established. The three-input version of the MIC in [25], is considered. Although the proposed converter appears to have more capacitors than the others, the capacitors on the non-coupled inductor side of the converter help to enhance the high output voltage delivery.

Table 3. Comparison between proposed converter and similar topologies

Three input converter	Switch count	Inductor count	Capacitor count	Diode count	Total count	Voltage gain	$V_{o,mode2}, V = 12V, d = 0.7$	Total cost
Boost/ switched capacitor- inductor [24]	5	5	5	7	22	$\frac{1}{1-d}$	226.66 V	Not reported
Switched inductor [25]	4	4	3	10	23	$\frac{1+2d}{(1-d)}$	102.45 V	\$ 97.32
Buck-boost/ Boost [26]	4	2	2	4	12	$\frac{1+d^2-d}{(1-d)^2}$	198.66 V	\$39.25
Boost/ boost [27]	4	2	2	4	12	$\frac{1+d}{(1-d)^2}$	161.33 V	Not reported
This work Boost/non-coupled inductor	4	3	4	5	16	$\frac{9}{2(1-d)}$	324 V	\$ 51.67

The converter by [26] shows a smaller voltage gain than the proposed converter, despite boasting of lower total component counts. Ref. [25] claimed a large voltage gain, however this can also be attributable to the maximum component count. Therefore, it can be speculated that [25] will have the highest cost.

In conducting a cost comparison between the proposed converter and the contemporary converters, the price estimates of the reported components of each converter have been culled from the Mouser website.

For the reported converters, [25] has been confirmed to have the highest cost, while [26] has the lowest cost. The cost of the proposed converter is lower than that of [25] but has a 31.6 % higher cost than [26]. It should be noted that the voltage output of [26] is lower than that of the proposed converter.

The converter proposed in [24] has the lowest voltage gain and the second-highest parts count. The Ref. [27] system, in comparison, has a high voltage gain while having the fewest parts—a tie with [26]. Due to the high voltage stress on the semiconductor devices and the large number of passive parts (mostly resistors) in the converter described by [26], [27], these converters have high losses. The output voltage during the operation mode 2 has been computed for the compared converters. It can be concluded that the proposed converter delivered the highest output voltage during the battery discharging operation mode.

#### 4. CONCLUSION

In this paper, a battery integrated three input high gain converter has been presented. The topology is based on the non-coupled inductor/ boost technique. The core merit of the converter is high voltage gain in the battery bypassed and battery discharging modes due to the non-coupled inductor topology. There is also a wide output voltage range. The battery port makes it suitable for RE applications. The operation modes have been defined. The output voltages in all modes are derived same as the inductor/ battery currents and voltage stresses. A power management algorithm has been proposed to switch the converter between working states dependent on the available RE sources. The proposed converter can serve PV/FC and battery inputs. The experimental results conform with the theoretical analysis of the converter. Future research may focus on mitigating losses associated with voltage stresses and current spikes during converter operation while maintaining the advantage of high voltage gain. Also, a model predictive control and battery management system could be investigated.

#### ACKNOWLEDGEMENTS

The authors are grateful and acknowledge the RIEC, Universiti Malaysia Sarawak (UNIMAS), for the financial support to undergo this research grant (UNI/F02/VC-HIRG/85525/P15-01/202).





#### REFERENCES

- [1] S. Khosrogorji, M. Ahmadian, H. Torkaman, and S. Soori, "Multi-input DC / DC converters in connection with distributed generation units – A review Multi-input DC / DC converters in connection with distributed generation units – A review," *Renew. Sustain. Energy Rev.*, vol. 66, no. December 2016, pp. 360–379, 2017, doi: 10.1016/j.rser.2016.07.023.
- [2] C. A. John, L. S. Tan, J. Tan, P. L. Kiew, A. M. Shariff, and H. N. Abdul Halim, "Selection of Renewable Energy in Rural Area Via Life Cycle Assessment-Analytical Hierarchy Process (LCA-AHP): A Case Study of Tatau, Sarawak," *Sustainability*, vol. 13, no. 21. 2021, doi: 10.3390/su132111880.
- [3] K. Jyotheeswara Reddy and S. Natarajan, "Energy sources and multi-input DC-DC converters used in hybrid electric vehicle applications – A review," *Int. J. Hydrogen Energy*, vol. 43, no. 36, pp. 17387–17408, 2018, doi: 10.1016/j.ijhydene.2018.07.076.
- [4] Y. M. Y. Buswig, A. Affam, A. K. H. Bin Othman, N. Bin Julai, Y. S. Sim, and W. Mulyo Utomo, "Sizing of a Hybrid Photovoltaic-Hydrokinetic Turbine Renewable Energy System in East Malaysia," *2020 13th Int. UNIMAS Eng. Conf. EnCon 2020*, 2020, doi: 10.1109/EnCon51501.2020.9299329.
- [5] Y. Ye and K. W. E. Cheng, "Multi-port voltage-subtracting circuit based on resonant switched-capacitor," *IET Power Electron.*, vol. 5, no. 6, pp. 693–701, 2012, doi: 10.1049/iet-pel.2011.0049.
- [6] Y. M. Ye and K. W. E. Cheng, "Multi-input voltage-summation converter based on switched-capacitor," *IET Power Electron.*, vol. 6, no. 9, pp. 1909–1916, 2013, doi: 10.1049/iet-pel.2013.0015.
- [7] S. Hou, J. Chen, T. Sun, and X. Bi, "Multi-input Step-Up Converters Based on the Switched-Diode-Capacitor Voltage Accumulator," *IEEE Trans. Power Electron.*, vol. 31, no. 1, pp. 381–393, 2016, doi: 10.1109/TPEL.2015.2399853.
- [8] A. Shoaie, K. Abbaszadeh, and H. Allahyari, "A Single-Inductor Multi-Input Multilevel High Step-Up DC–DC Converter Based on Switched-Diode-Capacitor Cells for PV Applications," *IEEE J. Emerg. Sel. Top. Ind. Electron.*, vol. 4, no. 1, pp. 18–27, 2022, doi: 10.1109/jestie.2022.3173178.
- [9] E. Amiri, R. R. Khorasani, E. Adib, and A. Khoshkbar-Sadigh, "Multi-Input High Step-Up DC-DC Converter with Independent Control of Voltage and Power for Hybrid Renewable Energy Systems," *IEEE Trans. Ind. Electron.*, vol. 68, no. 12, pp. 12079–12087, 2021, doi: 10.1109/TIE.2020.3047038.
- [10] Z. Saadatizadeh, P. C. Heris, X. Liang, and E. Babaei, "Expandable Non-Isolated Multi-Input Single-Output DC-DC Converter with High Voltage Gain and Zero-Ripple Input Currents," *IEEE Access*, vol. 9, pp. 169193–169219, 2021, doi: 10.1109/ACCESS.2021.3137126.
- [11] I. N. Jiya, H. Van Khang, A. Salem, N. Kishor, and R. Ciric, "Novel Isolated Multiple-Input Buck-Boost DC-DC Converter for Renewable Energy Sources," *IECON Proc. (Industrial Electron. Conf.)*, vol. 2021-October, pp. 1–6, 2021, doi: 10.1109/IECON48115.2021.9589538.
- [12] M. Veerachary and A. Trivedi, "Linear Matrix Inequality-Based Multivariable Controller Design for Boost Cascaded Charge-Pump-Based Double-Input DC-DC Converter," *IEEE Trans. Ind. Appl.*, vol. 58, no. 6, pp. 7515–7528, 2022, doi: 10.1109/TIA.2022.3201173.
- [13] S. Harini, N. Chellammal, B. Chokkalingam, and L. Mihet-Popa, "A Novel High Gain Dual Input Single Output Z-Quasi Resonant (ZQR) DC/DC Converter for Off-Board EV Charging," *IEEE Access*, vol. 10, no. June, pp. 83350–83367, 2022, doi: 10.1109/ACCESS.2022.3195936.





- [14] B. Chandrasekar *et al.*, "Non-Isolated High-Gain Triple Port DC-DC Buck-Boost Converter with Positive Output Voltage for Photovoltaic Applications," *IEEE Access*, vol. 8, pp. 113649–113666, 2020, doi: 10.1109/ACCESS.2020.3003192.
- [15] V. A. K. Prabhala, P. Fajri, V. S. P. Gouribhatla, B. P. Baddipadiga, and M. Ferdowsi, "A DC-DC Converter with High Voltage Gain and Two Input Boost Stages," *IEEE Trans. Power Electron.*, vol. 31, no. 6, pp. 4206–4215, 2016, doi: 10.1109/TPEL.2015.2476377.
- [16] A. Affam, Y. M. Y. Buswig, A. H. Othman, N. Julai, and H. Albalawi, "A battery integrated multiple input DC-DC boost converter," vol. 12, no. 2, 2023, doi: 10.11591/eei.v12i2.4272.
- [17] P. Mohseni, S. H. Hosseini, M. Sabahi, T. Jalilzadeh, and M. Maalandish, "A new high step-up multi-input multi-output DC-DC converter," *IEEE Trans. Ind. Electron.*, vol. 66, no. 7, pp. 5197–5208, 2019, doi: 10.1109/TIE.2018.2868281.
- [18] B. Zhu, Q. Zeng, D. M. Vilathgamuwa, Y. Li, and X. She, "Non-isolated high-voltage gain dual-input DC/DC converter with a ZVT auxiliary circuit," *IET Power Electron.*, vol. 12, no. 4, pp. 861–868, 2019, doi: 10.1049/iet-pel.2018.5465.
- [19] M. Dezhbord, P. Mohseni, S. H. Hosseini, D. Mirabbasi, and M. R. Islam, "A High Step-Up Three-Port DC–DC Converter With Reduced Voltage Stress for Hybrid Energy Systems," *IEEE J. Emerg. Sel. Top. Ind. Electron.*, vol. 3, no. 4, pp. 998–1009, 2022, doi: 10.1109/jestie.2022.3146056.
- [20] T. Jalilzadeh, N. Rostami, E. Babaei, and S. H. Hosseini, "Multiport DC-DC Converter with Step-Up Capability and Reduced Voltage Stress on Switches/Diodes," *IEEE Trans. Power Electron.*, vol. 35, no. 11, pp. 11902–11915, 2020, doi: 10.1109/TPEL.2020.2982454.
- [21] S. Athikkal, G. G. Kumar, K. Sundaramoorthy, and A. Sankar, "Performance Analysis of Novel Bridge Type Dual Input DC-DC Converters," *IEEE Access*, vol. 5, pp. 15340–15353, 2017, doi: 10.1109/ACCESS.2017.2734328.
- [22] S. Athikkal, B. Chokkalingam, S. I. Ganesan, B. Lehman, and T. B. Lazzarin, "Performance Evaluation of a Dual-Input Hybrid Step-Up DC–DC Converter," *IEEE Trans. Ind. Appl.*, vol. 58, no. 3, pp. 3769–3782, 2022, doi: 10.1109/TIA.2022.3152973.
- [23] Gaurav, N. Jayaram, S. Halder, K. P. Panda, and S. V. K. Pulavarthi, "A Novel Design With Condensed Component of Multi-Input High Gain Nonisolated DC–DC Converter for Performance Enhancement in Carbon Neutral Energy Application," *IEEE J. Emerg. Sel. Top. Ind. Electron.*, vol. 4, no. 1, pp. 37–49, 2023, doi: 10.1109/JESTIE.2022.3211779.
- [24] B. Z. Ghavidel, E. Babaei, and S. H. Hosseini, "An Improved Three-Input DC-DC Boost Converter for Hybrid PV/FC/Battery and Bidirectional Load as Backup System for Smart Home," *2019 10th Int. Power Electron. Drive Syst. Technol. Conf. PEDSTC 2019*, pp. 533–538, 2019, doi: 10.1109/PEDSTC.2019.8697731.
- [25] M. E. S. Mahmoodieh and A. Deihimi, "Battery-integrated multi-input step-up converter for sustainable hybrid energy supply," *IET Power Electron.*, vol. 12, no. 4, pp. 777–789, 2019, doi: 10.1049/iet-pel.2018.5782.
- [26] F. Kardan, R. Alizadeh, and M. R. Banaei, "A New Three Input DC/DC Converter for Hybrid PV/FC/Battery Applications," *IEEE J. Emerg. Sel. Top. Power Electron.*, vol. 5, no. 4, pp. 1771–1778, 2017, doi: 10.1109/JESTPE.2017.2731816.
- [27] A. Alizadeh Asl, R. Alizadeh Asl, and S. Hossein Hosseini, "A New PV/FC/Battery DC-DC Converter," *2022 13th Power Electron. Drive Syst. Technol. Conf. PEDSTC 2022*, vol. 1, no. 3, pp. 41–45, 2022, doi: 10.1109/PEDSTC53976.2022.9767329.

## BIOGRAPHIES OF AUTHORS



**Azuka Affam**     received the B.Eng. degree in Electrical and Electronic Engineering from Michael Okpara University of Agriculture, Umudike, Nigeria in 2010, and the MSc degree in Electronic Systems Design Engineering from Universiti Sains Malaysia in 2017. He is currently pursuing the Ph.D. degree in power electronics and renewable energy integration at Universiti Malaysia Sarawak, Malaysia. His research interests mainly include multi-input dc-dc converters, energy harvesting, renewable energy integration and battery energy storage systems. He can be contacted at 18010014@siswa.unimas.my.



**Yonis M. Yonis Buswig**     received his B.Eng. degree from Omar Al-Mukhtar University, Libya, in 2008. The M.Sc. degree in electrical and electronics engineering from Tun Hussein Onn University of Malaysia (UTHM), Batu Pahat, Johor, Malaysia, in 2011. In 2015, he was awarded his Ph.D. degree from Department of Power Engineering, Faculty of Electrical Engineering, Tun Hussein Onn University of Malaysia (UTHM). Currently, he is a Lecturer in the Department of Electrical and Electronic Engineering, Faculty of Engineering, Universiti Malaysia Sarawak. His current research interests include the area of power electronics, renewable energy technology, and motor drives control. He can be contacted at byonis@unimas.my.

	<p><b>Al-Khalid Hj Othman</b>    graduated his first degree from Nottingham Trent University, U.K in 1995 with BEng. (Hons) in Electrical and Electronic Engineering, followed by MSc. in Information Technology (Digital) from Nottingham University, U.K. in 1996. He obtained his Doctor of Philosophy (PhD) in Engineering from Newcastle upon Tyne University, U.K. in 2007 with specialization in Underwater Acoustic Network Protocol. He is a Professor at Faculty of Engineering, Universiti Malaysia Sarawak (UNIMAS). His research interests are communication network protocol and renewable energy. He can be contacted at okhalid@unimas.my.</p>
	<p><b>Shanti Faridah Salleh</b>    is a distinguished professional known for her extensive qualifications and expertise in the realm of sustainability and environmental management. Her impressive credentials include being a Chartered Energy Engineer, recognized by the Institute of Energy and the UK Engineering Council. In addition, she holds the esteemed title of a Professional Technologist in Green Technology, acknowledged by the Malaysia Board of Technologists. Currently, she is holding the post as the Director of the Institute of Sustainable and Renewable Energy (ISuRE) at UNIMAS (University Malaysia Sarawak), where she spearheads initiatives aimed at fostering green growth and environmental sustainability. She can be contacted at sshanti@unimas.my.</p>
	<p><b>Hazrul Mohamed Basri</b>    received his Bachelor of Engineering and Master of Engineering in Electrical engineering both from Université de technologie de Belfort Montbéliard (UTBM), France in 2008 and 2010 respectively. He also received his Ph.D in electrical engineering from University Malaya in 2019. He is currently a senior lecturer in University Malaysia Sarawak (UNIMAS) with Department of Electrical and Electronics engineering since 2010. He was awarded by the Board of Engineers Malaysia (BEM) the title of a professional engineer (P.Eng) in electronics discipline in 2018. His research interest includes power electronics, solar PV, fuel cell and optimization technique. He can be contacted at mbhazrul@unimas.my or mbhazrul@ieee.org.</p>
	<p><b>Norhuzaimin Julai</b>    received his PhD in Electrical and Electronic Engineering from Newcastle University, UK in 2015. He is with the Department of Electrical and Electronics Engineering, Faculty of Engineering, Universiti Malaysia Sarawak. His research area of interest is in the soft error in integrated circuit (IC), sustainable energy and renewable energy. He is a Chartered Engineer with the Energy Institute UK. He can be contacted at jnorhuza@unimas.my.</p>
	<p><b>Kasumawati Lias</b>    received her PhD in electrical engineering from University Teknologi MARA in 2019. She is currently a senior lecturer in University Malaysia Sarawak (UNIMAS) with Department of Electrical and Electronics engineering since 2006. She was awarded by the Board of Engineers Malaysia (BEM) the title of a professional engineer (P.Eng) in electronics discipline in 2020. Her research interest includes biomedical engineering, IoT Technology, Risk Assessment and Electromagnetics. She can be contacted at lkasumawati@unimas.my.</p>